JACS
JOURNAL OF THE AMERICAN CHEMICAL SOCIETY

Article

pubs.acs.org/JACS

Three-Dimensional Packing Structure and Electronic Properties of Biaxially Oriented Poly(2,5-bis(3-alkylthiophene-2-yl)thieno-[3,2-*b*]thiophene) Films

Eunkyung Cho,[†,‡] Chad Risko,[†] Dongwook Kim,[†,#] Roman Gysel,[§] Nichole Cates Miller,[§] Dag W. Breiby,[⊥] Michael D. McGehee,[§] Michael F. Toney,[∥] R. Joseph Kline,[▽] and Jean-Luc Bredas*[,†,⊗]

[†]School of Chemistry and Biochemistry and Center for Organic Photonics and Electronics, and [‡]School of Materials Science and Engineering, Georgia Institute of Technology, Atlanta, Georgia 30332, United States

[§]Department of Materials Science and Engineering, Stanford University, Stanford, California 94305, United States

[⊥]Department of Physics, Norwegian University of Science and Technology, Høgskoleringen 5, N-7491 Trondheim, Norway

[∥]Stanford Synchrotron Radiation Lightsource, Menlo Park, California 94025, United States

[▽]Polymers Division, National Institute of Standards and Technology, Gaithersburg, Maryland 20899, United States

Supporting Information

ABSTRACT: We use a systematic approach that combines experimental X-ray diffraction (XRD) and computational modeling based on molecular mechanics and two-dimensional XRD simulations to develop a detailed model of the molecular-scale packing structure of poly(2,5-bis (3-tetradecylthiophene-2-yl)thieno[3,2-*b*]thiophene) (PBTTT-C_{14}) films. Both uniaxially and biaxially aligned films are used in this comparison and lead to an improved understanding of the molecular-scale orientation and crystal structure. We then examine how individual polymer components (i.e., conjugated backbone and alkyl side chains) contribute to the complete diffraction pattern, and how modest changes to a particular component orientation (e.g., backbone or side-chain tilt) influence the diffraction pattern. The effects on the polymer crystal structure of varying the alkyl side-chain length from C_{12} to C_{14} and C_{16} are also studied. The accurate determination of the three-dimensional polymer structure allows us to examine the PBTTT electronic band structure and intermolecular electronic couplings (transfer integrals) as a function of alkyl side-chain length. This combination of theoretical and experimental techniques proves to be an important tool to help establish the relationship between the structural and electronic properties of polymer thin films.

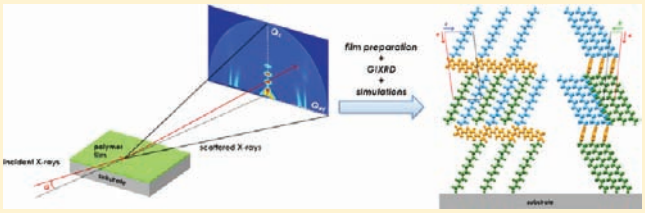

1. INTRODUCTION

The potential for low-cost, solution-based, high-throughput device fabrication makes π-conjugated polymers attractive materials as the active layer in organic-based electronics applications, including light-emitting diodes (OLEDs),[1,2] thin-film transistors (OTFTs),[3,4] and photovoltaics (OPVs).[5,6] Most polymers of interest in that context consist of two distinct constituents: (i) π-conjugated backbones that primarily determine the intrinsic electronic/optical properties and deliver structural rigidity and (ii) nonconjugated side groups that impart solubility to the polymer but also impact the packing structure, morphology, and microstructure of the polymer film, which are driven by kinetic and thermodynamic interactions during the spin-coating processing.[7−9] Chemical modification of these components provides tools for synthetic chemists with which to tune both the intrinsic and extrinsic polymer characteristics, and in turn influence the macroscopic material properties and impact overall device performance.

Polythiophenes, and in particular regioregular poly(3-hexylthiophene) (rr-P3HT), are among the most widely studied conjugated polymers for organic electronics applications.[10,11] Polythiophene thin films generally consist of ordered lamellar structures that define the material charge-transport pathways—typically along the linear conjugated backbones (intramolecular) and through the stacked π-conjugated backbones (intermolecular). Therefore, the polymer-chain orientation with respect to the electrodes can have considerable influence on the (opto)electronic characteristics of the device. In general, P3HT self-assembles into two-dimensional sheets in one of two primary orientations with respect to the substrate: (i) edge-on, where the lamella are parallel to the substrate, or (ii) face-on, where the lamella are perpendicular to the substrate. The orientation of the crystalline regions in the polymer film affects

Received: November 1, 2011
Published: February 29, 2012

   dx.doi.org/10.1021/ja210272z | *J. Am. Chem. Soc.* 2012, 134, 6177−6190

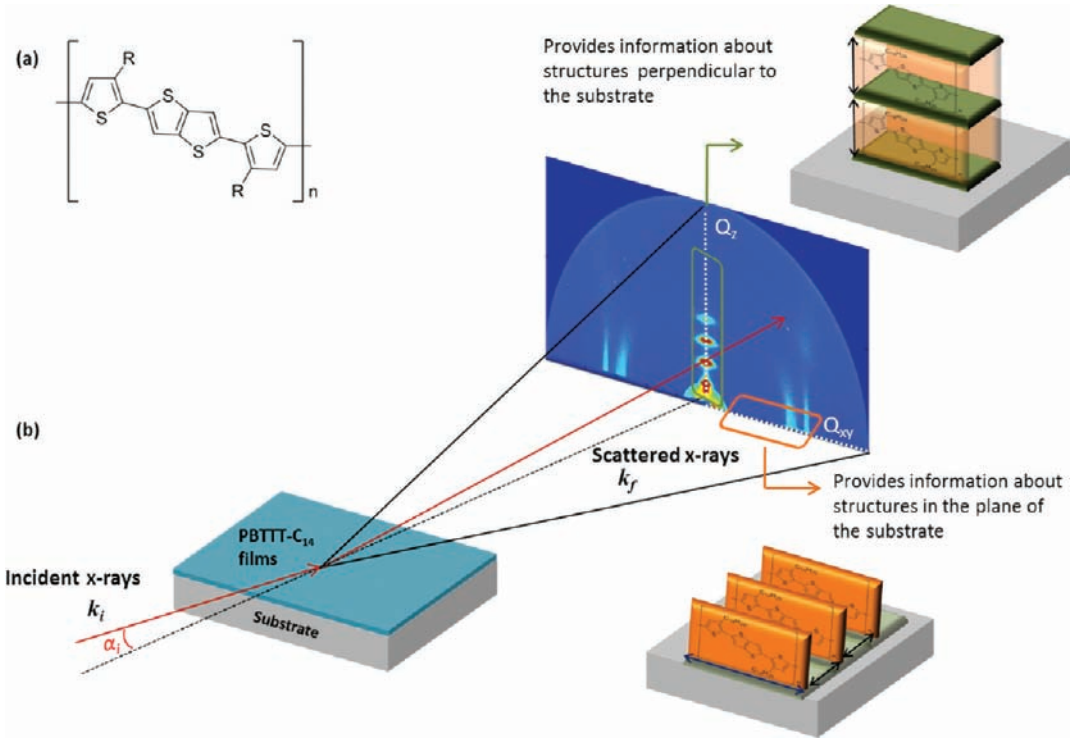

Figure 1. (a) Chemical structure of poly(2,5-bis(3-alkylthiophene-2-yl)thieno[3,2-*b*]thiophene) (PBTTT-C_n, where $C_n = C_8 - C_{18}$). (b) Schematic representation of grazing-incidence X-ray diffraction of PBTTT-C_{14} thin films; Q_{xy} and Q_z are the components of the scattering vector parallel and perpendicular to the substrate, respectively; diffraction peaks along Q_{xy} are due to periodic structures in the plane of the substrate (e.g., distance between the orange planes), and those along Q_z are due to the structures perpendicular to the substrate.

the charge-carrier mobilities measured in OTFT architectures: high mobilities of 0.05−0.1 $cm^2\ V^{-1}\ s^{-1}$ are observed for the edge-on orientation (as the $\pi-\pi$ stacking direction is parallel to the substrate), while films with face-on orientation tend to have a limited mobility of $2 \times 10^{-4}\ cm^2V^{-1}\ s^{-1}$;[11] it is noteworthy, however, that some high-performance polymer systems (i.e., poly{[*N*,*N*-9-bis(2-octyldodecyl)naphthalene-1,4,5,8-bis(dicarboximide)-2,6-diyl]-*alt*-5,59-(2,29-bithiophene)})[12,13] produce high charge-carrier mobilities in OTFT architectures even though they appear to predominantly present face-on orientations with respect to the substrate. Importantly, P3HT has also been widely used in OPV applications as the hole-transport (donor) material in bulk-heterojunction (BHJ) blends with methanofullerene-[6,6]-phenyl C_{61}-butyric acid methyl ester ($PC_{61}BM$, acceptor) to produce devices that exhibit power conversion efficiencies >5.0%.[14,15]

Poly(2,5-bis(3-alkylthiophene-2-yl)thieno[3,2-*b*]thiophene) (PBTTT-C_n)[16−21] has recently shown promise as an active-layer component for organic-based electronics applications due to its large hole mobility that reaches up to 1 $cm^2\ V^{-1}\ s^{-1}$ for PBTTT-C_{14} and PBTTT-C_{16} in OTFT architectures.[22,23] Moreover, BHJ solar cells consisting of a 1:4 blend of PBTTT-C_{14} and methanofullerene[6,6]-phenyl C_{71}-butyric acid methyl ester ($PC_{71}BM$) present a power conversion efficiency of 2.3%.[24,25] The features that lead to the improved charge-carrier mobilities compared with P3HT are attributed to increased structural ordering in PBTTT-C_n. As shown in Figure 1a, the PBTTT-C_n monomer consists of a thienothiophene unit appended on each side by a single thiophene unit that contains a long alkyl side chain (typically ranging from C_8H_{17} to $C_{18}H_{37}$). The initial structural analysis of the thin-film structure suggested that the PBTTT-C_n alkyl side chains are relatively well-ordered, allowing for interdigitation and the formation of closely packed lamellar structures.[16] Overall, this leads to enhanced three-dimensional ordering relative to P3HT (where the side-chain density is too large to permit inter-digitation and mostly results in two-dimensional ordering) and improved charge-carrier transport.[26−28]

With these differences in mind, it is of interest to understand how intermolecular interactions and packing in these polymers influence their nanostructured morphology and electronic properties. A number of experimental and theoretical efforts to investigate the relationship between morphology, supra-organization, and charge-carrier transport of PBTTT-C_n have been undertaken. Initial structural models were developed through evaluation of the polymer structure and intermolecular packing distance between adjacent planes through X-ray diffraction (XRD) techniques assuming an orthorhombic unit cell.[16,17] X-ray scattering from PBTTT-C_{12} and PBTTT-C_{14} thin films provides several relatively intense diffraction peaks along both the Q_z (perpendicular to the substrate) and Q_{xy} (parallel to the substrate) directions (see Figure 1b) and reflect the presence of considerably ordered crystalline domains. The structural models further evolved based on data from near-edge X-ray absorption fine structure (NEXAFS) and infrared (IR) absorption spectroscopies[26] that detailed the polymer backbone orientations and revealed the orientation of the alkyl side chains relative to the substrate normal: the conjugated backbone planes are slightly tilted (22°) with respect to the substrate plane, while the side chains are more substantially tilted (45°). These findings were verified by theoretical studies at the density functional theory (DFT) level in which the atomic and electronic structures of 2D sheets of PBTTT-C_6 were evaluated;[29] a slight backbone tilt (23°) with

dx.doi.org/10.1021/ja210272z | *J. Am. Chem. Soc.* 2012, 134, 6177−6190

respect to the substrate normal and interdigitation of the alkyl chains were determined to be energetically favorable features for polymer packing. Importantly, Brocorens et al. used molecular mechanics (MM) and XRD simulations to study the molecular packing of PBTTT-C_{12}, with a focus on the supra-organization of the polymer chains in the lamellae;[30] these studies led to the proposition that the unit cell is triclinic and provided estimates of the intermolecular electronic couplings. Recently, DeLongchamp et al. used a flow-coating technique to obtain biaxially aligned PBTTT-C_{14} films with in-plane texture to determine the in-plane crystal orientation, again based on an orthorhombic cell, via grazing incidence X-ray diffraction (GIXD).[31] While these empirical and theoretical models of PBTTT in the thin film provide important details concerning the polymer structure and packing, there remain a number of dissimilarities among the models, and the overall agreement with GIXD data is incomplete.

Here, using a combination of GIXD, well-ordered (biaxially aligned) films, and MM simulations, we assemble a detailed structural model of PBTTT-C_n (n = 12, 14, 16) and take steps toward developing a structure-based toolset for the description of semicrystalline polymer films. Details concerning the molecular orientation of PBTTT-C_{14} are determined through the theoretical analysis of the experimental diffraction images obtained for biaxially oriented films. Importantly, the combined MM and 2D XRD simulations are applied to the examination of how the polymer components (i.e., backbone and side chains) contribute to the total diffraction pattern, and how changes in the molecular orientation influence the diffraction pattern. Moreover, we examine how the length of the alkyl side chains, specifically in going from $C_{12}H_{25}$ to $C_{14}H_{29}$, and $C_{16}H_{33}$, affects the molecular packing. Finally, the influence of these parameters on the electronic band structure and intermolecular electronic couplings is evaluated. These results lead to a better understanding of the relationship between polymer packing and electronic structure and are an important step forward in unraveling the complexity of conjugated polymers.

2. EXPERIMENTAL SECTION

2.1. Material Preparation. PBTTT was synthesized as previously reported.[16] Isotropic in-plane films, i.e., films of "fiber texture" having a well-defined crystallographic direction along the film normal, yet with random orientation of crystallites about the normal, were spin-cast on OTS-treated silicon wafers from solutions of 5 mg/mL polymer in 1,2-dichlorobenzene. The films were then heated above the first phase transition into the mesophase[27] for 5 min at 180 °C and slowly cooled. Biaxially aligned films (in-plane and out-of-plane textured) were prepared by a previously reported flow-coating procedure[31] and deposited on UV-ozone-cleaned silicon wafers with a native oxide. Solutions of 15 mg/mL polymer in a 6:1 ratio of chloroform and 1,2-dichlorobenzene were heated to 80 °C until the polymer dissolved. The solution was cooled to 70 °C. A glass slide was mounted at a 15° angle from the silicon substrate. The gap between the slide and the substrate was about 150 μm; 12 μL of solution was dispensed between the slide and the substrate. The substrate was translated at 2 mm/s, leaving behind a thin film of solution. As the solvent evaporated, the drying front slowly progressed across the substrate. The film was completely dry within 1 min. The film was then heated at 250 °C for 5 min, followed by a slow cool to room temperature (5 °C/min). In the case of biaxial samples, a higher annealing temperature was used as the films have to be melted to obtain the biaxial samples. The film thicknesses were about 20 and 30 nm for the isotropic in-plane films and biaxially aligned films, respectively.

2.2. Characterization. GIXD measurements took place at the Stanford Synchrotron Radiation Lightsource (SSRL) at beamlines 7-2 and 11-3. The point detector GIXD was conducted on beamline 7-2. For these GIXD measurements, the films were illuminated with an 8 keV beam at a constant incidence angle of ~0.2°. For the biaxial samples with the in-plane preferred orientation, radial scans were obtained by keeping the direction of the scattering vector, $\mathbf{Q}$, aligned along the peak of interest. For ϕ-scans where the sample was rotated while maintaining the detector at a fixed position, a constant incidence angle was maintained as the sample was rotated. We define ϕ = 0° as the orientation when the scattering vector is perpendicular to the long axis of the molecular backbones and parallel to the π-stacking direction. Similarly, ϕ = 90° is the orientation when the scattering vector is oriented parallel to the long axis of the molecular backbones. The 2D GIXD measurements were conducted on beamline 11-3 with an image plate detector, an incident energy of 12.735 keV, and an incidence angle of ~0.12°. For area detector measurements, the biaxial samples were aligned relative to the *incident beam*. This orientation resulted in the scattering vector aligned away from the flow direction by the Bragg angle, θ_B. For the energy used, θ_B was 6.3° for the (1−13) and 7.6° for the (110) scattering peaks. These are both less than the full width at half-maximum (fwhm) observed in the ϕ-scans. All sample chambers were purged with helium flow during the scattering experiments to reduce beam damage and background scattering. Note that the intensities in the diffraction images will be shown on a logarithmic scale.

2.3. Computational Modeling. The initial crystal geometry for each polymer in the PBTTT-C_n series was taken as one monomer in a unit cell of varying lattice parameters and periodic boundary conditions; the a-axis was defined as a lamellar growth direction, the b-axis as the backbone stacking direction, and the c-axis as the monomer repeat direction along the polymer chain. Each monomer consisted of a planar backbone with the thiophene moieties oriented in *anti*-configurations with respect to the thienothiophenes. The alkyl side chains were extended into the neighboring (lamellar) unit cell to form interdigitated networks, as previously suggested.[30] All MM calculations were performed with the Materials Studio software suite. Atomic charges were assigned via the COMPASS force field. Three force fields commonly used to study organic materials—the Universal force field (UFF),[32] COMPASS,[33] and Dreiding[34]—were evaluated to determine their appropriateness to study the PBTTT-C_n series; the three force fields principally differ in the detailed energy functions and parameters that describe molecular interactions. The crystal structure of PBTTT-C_{12} has been previously examined using each of these force fields,[30] therefore allowing for direct comparison. Nonbonded interactions in the crystal structure were calculated by the Ewald method with an energy accuracy of 10^{-4} kcal/mol.[35]

The optimized polymer unit cells were used to simulate the 2D GIXD patterns using simDiffraction.[36,37] An incident X-ray wavelength of 0.975 Å (corresponding to an incident energy of 12.7 keV), a fixed incidence angle of 0.1°, and a peak width of 0.02 $Å^{-1}$ were used for the simulations. The simulated 2D XRD patterns are plotted in a space spanned by Q_{xy} (the scattering vector component parallel to the substrate) and Q_z (the scattering vector component perpendicular to the substrate). The (h00) planes of the crystalline domains were set to be preferentially oriented parallel to the substrate, as this edge-on orientation is found experimentally.[16] The intensity of the diffraction peaks was calculated by

$$I_{hkl}(Q) = \sum_{W_i} [CLP|F(Q)|^2 DW\ \Omega] \quad (1)$$

where the summation runs over all crystallite orientations W_i, and C is a constant that depends on the incident flux along with other factors. The Lorentz (L), in-plane polarization (P), structure (F), and Debye−Waller (DW) factors were each taken into account to calculate the peak intensities in the simulations:

$$L = \frac{1}{\cos \alpha_i \sin \psi \cos \beta} \quad (2)$$

$$P = \cos^2 \beta \cos^2 \psi + \sin^2 \beta \quad (3)$$

dx.doi.org/10.1021/ja210272z | J. Am. Chem. Soc. 2012, 134, 6177−6190

$$F(Q) = \sum_i f_i(Q) \exp[2\pi i(hx_i + ky_i + lz_i)] \quad (4)$$

$$DW = \exp(-u^2Q^2) \quad (5)$$

where α_i, ψ, and β denote the incidence angle, the in-plane scattering angle, and the exit angle, respectively, as described elsewhere;[38] f_i, the atomic form factor; x_i, y_i, and z_i, the relative atomic positions; h, k, and l, the Miller indices; and u, the root-mean-square displacement of atoms induced by static disorder and thermal vibrations (set to 0.2 Å).

The crystallite orientational distribution function (ODF), Ω, was used to describe the in-plane and out-of plane preferential orientations of the thin films and is given by both the degree of in-plane orientation ($W_{\|}$) and the degree of out-of-plane orientation ($W_{\perp}$):

$$\Omega(W_{\|}, W_{\perp}) = \frac{1}{n}\exp\left(\frac{-2\ln 2\omega_{\|}^2}{W_{\|}^2}\right)\exp\left(\frac{-2\ln 2\omega_{\perp}^2}{W_{\perp}^2}\right) \quad (6)$$

where N is a normalization factor, and $\omega_{\|}$ and $\omega_{\perp}$ indicate the orientation angles with respect to the in-plane and sample normal directions, respectively. Small $W_{\|}$ or $W_{\perp}$ values, which indicate a narrow distribution of crystallite orientations with respect to the preferential direction, were used in accordance with the narrow orientational distribution functions measured experimentally. The rocking angle was set to zero in these simulations so as to clearly identify the diffracted spots. Therefore, no (h00) peaks are observed in the simulated XRD patterns since the Bragg condition at a fixed incidence angle is not satisfied.

Based on the results of force-field evaluation (see the Supporting Information), UFF was selected for the analysis of the PBTTT-C$_n$ series, a result consistent with the work of Brocorens et al.[30] We note that the UFF parameters that we used were those that were slightly modified in ref 30, as these lead to a better reproduction of the planarity of the conjugated backbone. No further modifications to the force field were made.

Although the initial structural model derived by the UFF calculations provides reasonable agreement with respect to the experimental data, a number of discrepancies exist between the simulated and experimental XRD patterns, in terms of the (exact) peak positions. Therefore, we varied the unit-cell lattice parameters (a, b, c, α, β, and γ); for each given set of lattice parameters, the polymer structure was completely optimized. The 2D XRD patterns of the new structures were then simulated and compared to experiment, which allowed us to eventually refine the unit-cell parameters and packing structure of the polymer.

DFT was used to evaluate the electronic properties of the optimized polymers, with the molecular geometries taken from the refined model without further geometry optimization. Intermolecular transfer integrals (electronic couplings) between adjacent polymer chains were determined using the B3LYP functional[39−41] and the 6-31G(d,p) basis set;[42−44] detailed computational methods concerning the evaluation of the transfer integrals are described elsewhere in the literature.[45] All nonperiodic DFT calculations were carried out with the Gaussian 09 program suite.[46] Electronic band structures were determined using DFT at the B3LYP/6-31G(d) level within the CRYSTAL06 program;[47] the Monkhorst−Pack scheme for 2×8×4 k-point mesh in the Brillouin zone was applied.

3. RESULTS AND DISCUSSION

In the following, we present the key procedures and results of the structural model development for the PBTTT-C$_n$ series. The GIXD data for PBTTT-C$_{14}$ films with random in-plane orientations are analyzed via a series of MM and XRD simulations to provide the initial structural details of the PBTTT-C$_{14}$ model. The same techniques are then applied to further test and refine the model through the analysis of biaxially aligned thin films. With this model, we then examine how the individual polymer components (i.e., conjugated backbone and alkyl side chains) contribute to the XRD pattern. We then assess the discrepancies between the model structure and previous spectroscopic data concerning particular aspects of the polymer orientation. Finally, we use the model structures to evaluate the electronic band structure (and intermolecular electronic couplings) of the polymers and determine how the differences in the alkyl side-chain lengths affect the charge-transport characteristics.

3.1. Uniaxially Oriented PBTTT-C$_{14}$ Films with Random In-Plane Orientation. The accurate determination of molecular orientation, packing, and unit-cell parameters is of critical importance to evaluate the charge-carrier transport properties of organic electronic materials, as charge-carrier transport is highly dependent on the both intra- and intermolecular interactions.[48] Based on the empirical and theoretical methodology described above, the packing structure of PBTTT-C$_{14}$ was determined (at 0 K) and is shown in Figure 2.

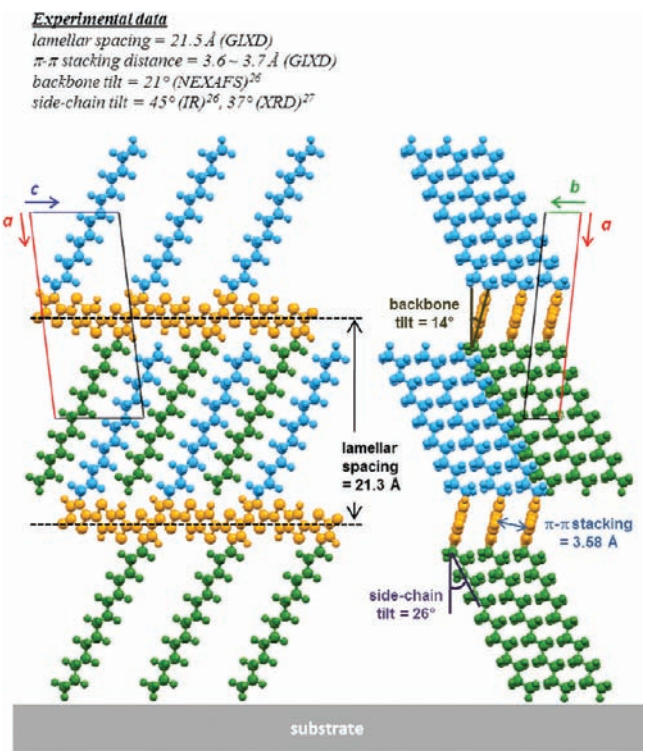

Figure 2. Out-of-plane packing motifs for the simulated model of PBTTT-C$_{14}$ viewed along the b-axis (left) and c-axis (right); the color coding is such that orange represents the polymer backbones and blue and green represent the side chains attached above and below the backbones, respectively. The substrate is shown to indicate the polymer film orientation, as it is not completely known how the PBTTT layer next to the substrate is aligned.

The unit cell is triclinic, with unit-cell parameters a = 21.5 Å, b = 5.4 Å, c = 13.5 Å, α = 137°, β = 86°, γ = 89°. These unit-cell parameters are similar to those previously proposed for PBTTT-C$_{12}$.[30] The conjugated backbones are planar, with a slight tilt (14°) of the short backbone axis with respect to the substrate normal; this tilt is in reasonable agreement with, though somewhat smaller than, the backbone tilt (21° ± 3°) obtained from NEXAFS.[26] We note that the NEXAFS measurement is an azimuthal average of unknown orientation distribution and requires the assumption of a single, narrow tilt distribution to calculate the tilt angle; if disorder is present in the film, the estimated tilt will shift toward the magic angle

dx.doi.org/10.1021/ja210272z | J. Am. Chem. Soc. 2012, 134, 6177−6190

(54.7°) and result in an estimated tilt larger than that in the ordered regions. The inter-backbone stacking distance (π-stacking distance) is relatively short, at 3.58 Å; coupled with the planar backbones, this should lead to strong electronic communication along the *b*-axis (*vide infra*). The interdigitated alkyl side chains are straight, leading to the formation of lamellar structures with a *d*-spacing of 21.3 Å. The tilt of the side chains from the substrate normal is 26°. This result is substantially smaller than the 45° tilt determined from polarized IR spectroscopy[26] but closer to the 37° tilt estimated with XRD from the change of lamellar spacing with side-chain length.[27] As was previously described for NEXAFS, IR spectroscopy also measures an azimuthal average of an unknown distribution, and this skews the estimated tilt angle toward the magic angle of 54.7° when disorder is present, as for semicrystalline polymers. Therefore, the IR-derived tilt is likely overestimated for PBTTT. The sensitivity of the simulated XRD pattern to side-chain tilt will be discussed in more detail below. In general, there is good agreement among the empirically determined and modeled orientation and distance parameters.

Figure 3 shows the experimental and simulated XRD patterns of PBTTT-C_{14} with random in-plane orientation; the position and index of the experimental and simulated peaks are compared in Table 1. PBTTT, after solution deposition and annealing, forms a highly textured film that has both strong preferential orientation with respect to the substrate normal and random in-plane orientations.[17] Bearing this in mind for the XRD simulations, the crystal domains were set to be preferentially (100) oriented along Q_z (uniaxial alignment), and the parameters for the in-plane ($W_{\|}$) and out-of-plane ($W_{\perp}$) orientations were set to infinity and 2° (fwhm = 2°), respectively, to reflect the thin-film orientational distribution. As shown in Figure 3, the simulated XRD patterns have no observable (*h*00) Bragg peaks, since the crystal unit cell was set to be well aligned with respect to the substrate plane.[49,50] We find good agreement between the empirical and simulated data, as there are strong peaks at Q_{xy} = 1.41 and 1.71 Å^{-1} that reflect the lateral ordering of the polymer films. All nonspecular reflections are observed in the experiments and simulations in Figure 3 since the films are isotropic in-plane. Therefore, further analysis is necessary to separate these peaks and to develop a more robust model.

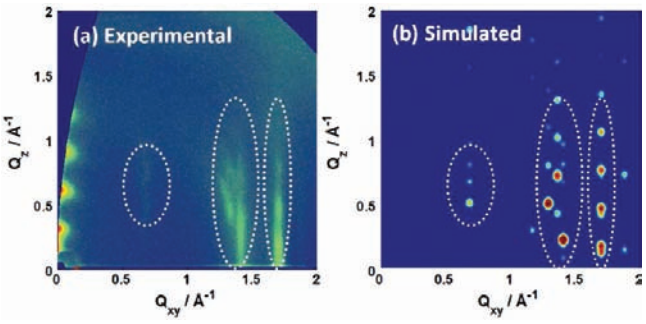

Figure 3. Experimental (a) and simulated (b) XRD patterns of PBTTT-C_{14} with random in-plane orientation. Dotted ellipses on the experimental diffraction pattern are transposed to the simulated spectra to serve as a guide to the eye. All intensities are shown on a logarithmic scale.

Table 1. Indexing of the Intense Peaks in Uniaxial PBTTT-C_{14}[a]

experiment	simulated model		
Q_{xy} (Å^{-1})	(*hkl*)	Q_{xy} (Å^{-1})	Q_z (Å^{-1})
1.29	(21−1)	1.29	0.50
1.35	(302)	1.37	0.72
1.41	(1−13)	1.41	0.22
1.71	(0−10)	1.71	0.17
	(110)	1.71	0.12
1.71	(1−10)	1.71	0.47
	(210)	1.71	0.42
1.71	(2−10)	1.71	0.76

[a]The experimental error bars for Q_{xy} are ±0.01 Å^{-1}.

3.2. Biaxially Oriented PBTTT-C_{14} Films. The application of a flow-coating procedure followed by thermal annealing produces films of PBTTT-C_{14} in which the backbone orientation is aligned preferentially in-plane along the flow direction (with some distribution in the substrate plane).[31] Such additional control over the film morphology leads to biaxially oriented films as the (*h*00) lamellar domains remain strongly oriented perpendicular to the substrate. Figure 4 depicts the in-plane orientation via a top-view derived from the modeled unit cell. The polymer backbones (orange) are well-aligned within the *b*−*c* plane (parallel to the substrate plane). Interestingly, the conjugated backbones are displaced by 3.68 Å (from a perfect cofacial orientation) with respect to their neighbors along the long axis, while maintaining a short inter-backbone packing distance (3.58 Å). We note that this

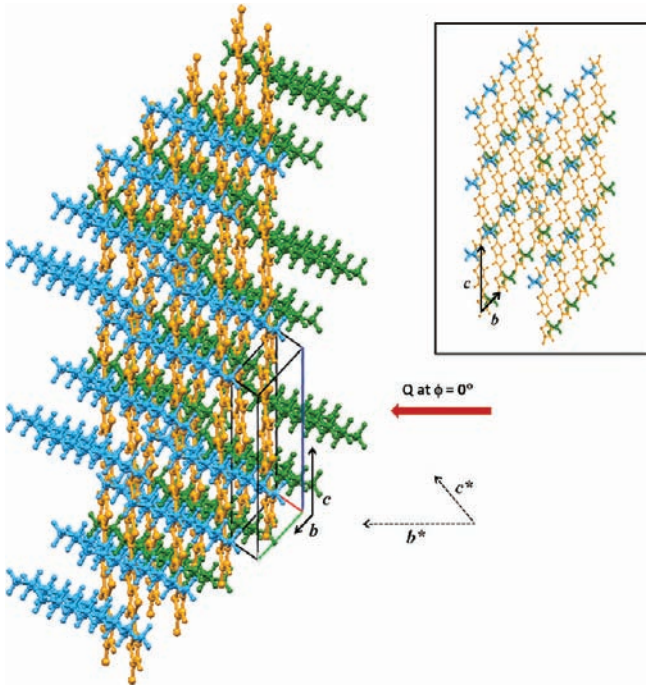

Figure 4. In-plane orientation of the PBTTT-C_{14} model viewed along the *a**-axis. Orange represents the polymer backbones; blue and green represent the side chains attached above and below the backbones, respectively; solid and dotted arrows indicate axes of direct and reciprocal lattice, respectively; a thick red arrow represents the scattering vector **Q** at the azimuthal angle ϕ = 0° for the GIXD data. The inset highlights the molecular structure viewed along the side chains to clearly show the backbone orientations relative to the side chains.

dx.doi.org/10.1021/ja210272z | J. Am. Chem. Soc. 2012, 134, 6177−6190

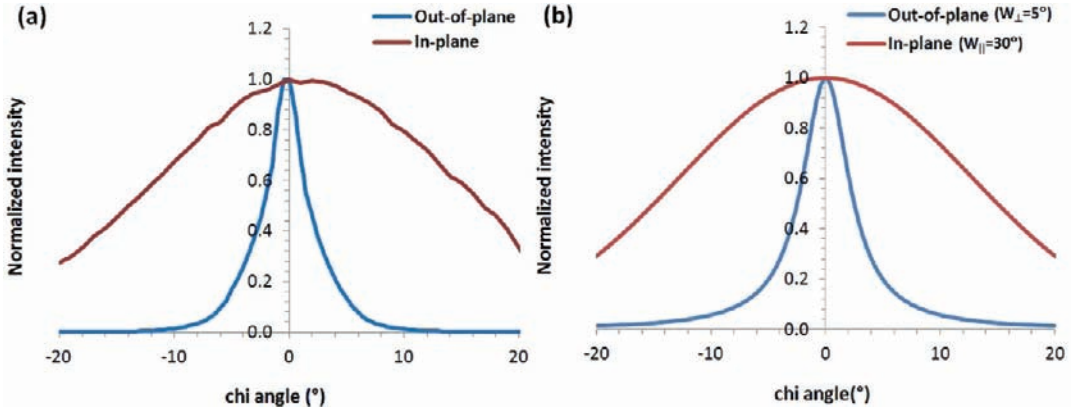

Figure 5. Experimental (a) and simulated (b) orientation distributions of biaxially oriented PBTTT-C_{14} film for the out-of-plane ((100), blue) and in-plane ((110), red) directions.

displacement along the long axis differs from previous results obtained at the quantum-mechanical DFT level[29] and has a direct impact on the electronic properties of the polymer (see below). The alkyl side chains have a preferential in-plane rotation with respect to the backbone of about 58°.

The in-plane orientation of the biaxial films can be detected by GIXD measurements. As stated earlier, the azimuthal angle (ϕ) is the angle between the in-plane component of scattering vector (Q_{xy}) and the in-plane component of b^*. At 0°, the (h10) peaks corresponding to the inter-chain backbone stacking are strongly observed. However, the specific reflections that occur at various ϕ angles (e.g., 45° and 90°) depend on the unit-cell parameters for the triclinic cell. For example, the (h01) peaks appear near angle $\phi = \alpha^*$, the angle between b^* and c^*.

XRD simulations were performed at different in-plane orientations (azimuthal angles ϕ) to confirm the validity of the detailed in-plane packing of the PBTTT-C_{14} model. To account for both the strong out-of-plane orientation and the preferential in-plane orientation of the flow-coated biaxially aligned film, the parameters for out-of-plane ($W_\perp$) and in-plane ($W_\parallel$) orientations were obtained from the experimental data. Figure 5 shows the experimental out-of-plane and in-plane orientation distributions obtained from the (100) and (110) peaks, respectively, and demonstrate that the out-of-plane orientation is much narrower than the in-plane orientation. The out-of-plane and in-plane orientation distribution functions are determined by comparison with the experimental orientation distribution functions and we find $W_\perp = 5°$ and $W_\parallel = 30°$ by inspection. Simulated XRD patterns at the ϕ angle were averaged at $-\phi$, ϕ+180° and $-\phi$+180° to reflect symmetry-related deviations in backbone orientation with respect to the (empirical) preferential direction.

Figure 6 and Table 2 display the empirical and simulated XRD patterns and peak positions for the biaxial films at various azimuthal angles.[51] Note that, as explained in the Experimental Section, the samples were aligned relative to the *incident beam* direction. Thus, Q_{xy} was not along a high symmetry direction but rather is tilted by θ_{Bragg}. However, since θ_{Bragg} is, in general, less than the fwhm of the in-plane orientation (30°), we label the GIXD patterns by the nominal ϕ. The simulated patterns show good agreement with the experimental data in terms of dominant peak positions. At the azimuthal angle $\phi = 0°$ (backbones parallel to the beam direction), the (h10) peaks appear strong at $Q_{xy} = 1.71$ Å^{-1} with intensity along Q_z. As Figure 7 shows, the Q_z values for (h10) peaks obtained from the simulation are consistent with the (broader) experimental peaks. In this region, each spot comes from a contribution of two reflection planes; the peaks at $Q_z = 0.15$ Å^{-1} are from the (0−10) and (110) planes, those at $Q_z = 0.47$ Å^{-1} from the (1−10) and (210) planes, and those at $Q_z = 0.79$ Å^{-1} from the (2−10) and (310) planes. The difference between any two pairs of reflection planes along Q_z is only 0.05 Å^{-1}, so the two peaks appear as one broader peak. As the simulated XRD pattern shows distinct spots for the aligned crystalline domains, it is anticipated that stacking faults and disorder in the films are the cause for the smeared and broad peaks present in the experimental data; indeed, X-ray line-shape analysis of PBTTT reveals considerable para-crystalline disorder along the π−π stacking direction, which can influence the charge-transport properties.[52] Because of the broad in-plane orientation distribution, the (21−1) reflection is also observed, even though it is centered at $\phi = 14°$ in the simulations. Additionally, analyses of the simulated XRD patterns provide a clear interpretation of the intense peaks at $\phi = 45°$ and 90°. At 45°, the (201) and (302) peaks are intense as $\alpha^* = 48°$; thus, the scattering vector lies nearly parallel to the c^* direction at this azimuthal angle; at 90°, the mixed reflection planes (1−13) and (3−14) appear.

Polymer films provide few GIXD peaks, and it is generally difficult, to say the least, to perform structural refinements. It is thus important to stress that having available at the same time (i) a biaxially oriented polymer film, (ii) precise GIXD measurements, and (iii) XRD simulations provides a powerful approach to fully describe the packing arrangement of PBTTT-C_{14}. Our results also underscore that it is only through such rigorous combinations that good structural models of polymer thin films can be attained.

3.3. Influence of the Molecular Packing on the XRD Patterns. Based on the modeling techniques described here, it is very useful to establish if more detailed information pertaining to the contributions to the XRD pattern from the individual polymer components, that is, the polymer-conjugated backbone or the alkyl chains, can be acquired. Figure 8 displays the simulated XRD patterns for the individual polymer components for three in-plane azimuthal angles. The contributions from each component of the polymer structure were evaluated by setting all atoms on the polymer component not of interest to be non-diffracting (i.e., hydrogen-like). We note that the component definitions are somewhat arbitrary and that, by "removing" one of the components, peaks due to interference could be missed. Contributions from the polymer backbones and from the side chains are readily identifiable in

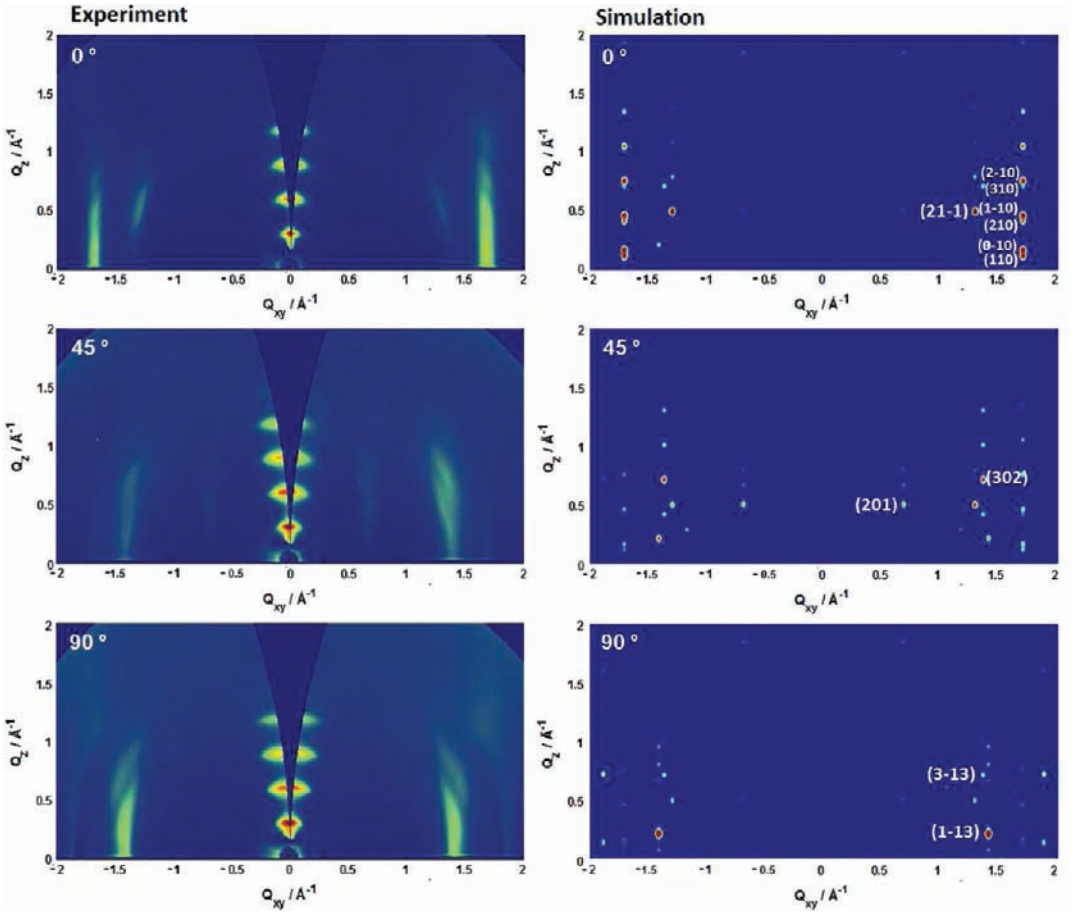

Figure 6. Comparison of experimental (left) and simulated (right) XRD diffraction patterns of biaxial PBTTT-C_{14} films at various azimuthal angles (ϕ = 0°, 45°, 90°) with respect to the incident beam direction. The experimental diffraction images at 0° and 90° are not symmetric since the samples are aligned with ±2° deviation. When the samples are misoriented, you can see asymmetry in the films. The peaks near 45° are much broader than the peaks near 0° or 90°. Intensities are shown on a logarithmic scale.

Table 2. XRD Peak Indexing for the Experimental and Simulated Biaxial PBTTT-C_{14} Films at Various Azimuthal Angles (ϕ = 0°, 45°, 90°) with Respect to the Incident Beam Direction[a]

	experiment		simulated model		
ϕ	Q_{xy} (Å^{-1})	Q_z (Å^{-1})	(hkl)	Q_{xy} (Å^{-1})	Q_z (Å^{-1})
0°	1.29	0.50	(21−1)	1.29	0.50
	1.71	0.15	(0−10)	1.71	0.17
			(110)	1.71	0.12
	1.71	0.47	(1−10)	1.71	0.47
			(210)	1.71	0.42
	1.71	0.79	(2−10)	1.71	0.76
			(310)	1.71	0.71
45°	0.68	0.51	(201)	0.68	0.51
	1.35	0.73	(302)	1.37	0.72
90°	1.41	0.30	(1−13)	1.41	0.22
	1.41	0.74	(3−13)	1.41	0.81

[a]The experimental error bars for Q_{xy} are ±0.01 Å^{-1}.

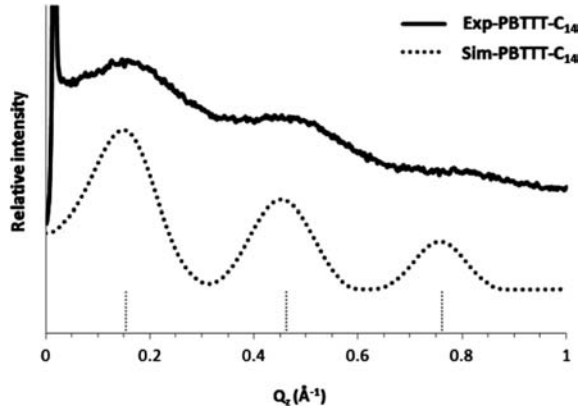

Figure 7. Experimental (solid line) and simulated (dotted line) plots of (h10) peak intensities at Q_{xy} = 1.71 Å^{-1} for PBTTT-C_{14} vs Q_z; the short dotted vertical lines represent the expected Q_z positions. The simulated data were broadened with a Gaussian function (fwhm = 2×original fwhm).

Figure 8 and for the films without in-plane ordering in the Supporting Information. The backbones mainly contribute to the diffraction peaks at Q_{xy} = 1.71 Å^{-1} (π-stacking peaks), while the side chains make significant contributions to the peaks around Q_{xy} = 1.29−1.41 Å^{-1}. These results suggest that the degree of disorder for the different components plays a significant role in the intensity of the XRD pattern. Indeed, one would expect *a priori* that diffraction peaks arising from the more flexible and disordered alkyl side chains would be weaker and more diffuse than those mainly arising from the conjugated backbone, a result borne out by the analysis of the partitioned structure. In terms of azimuthal angle dependence of the

dx.doi.org/10.1021/ja210272z | J. Am. Chem. Soc. 2012, 134, 6177−6190

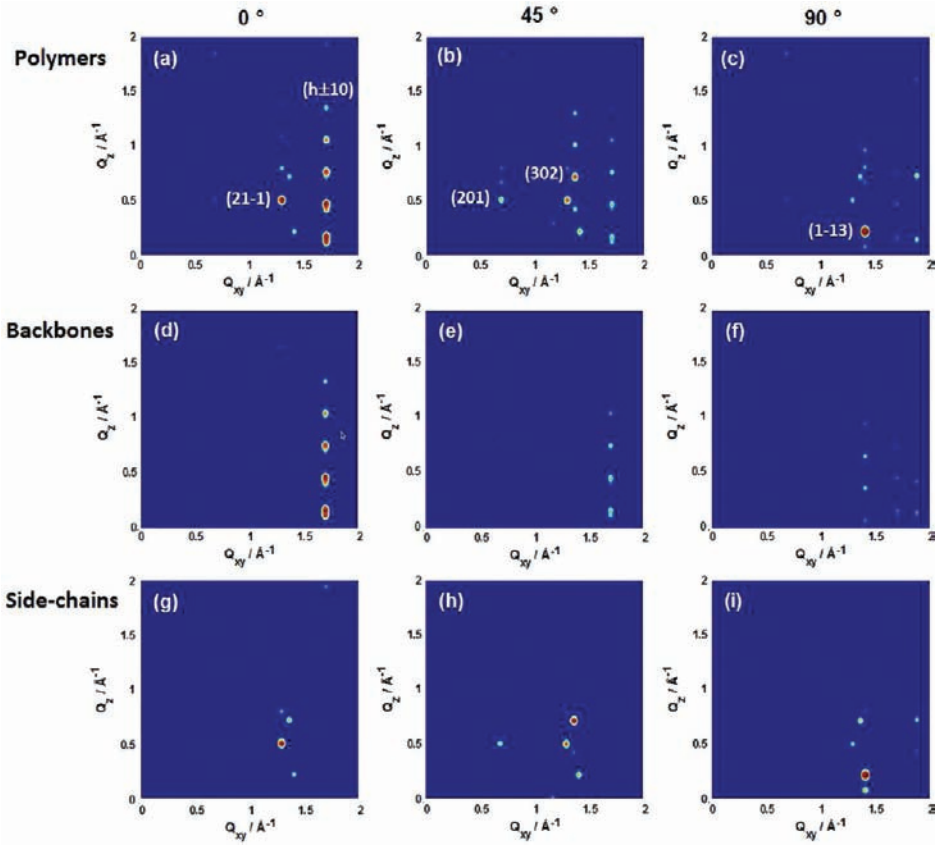

Figure 8. Simulated XRD patterns at azimuthal angles (ϕ = 0°, 45°, 90°) with respect to the incident beam direction for the biaxial PBTTT-C_{14} polymer (a–c), backbone segments (d–f), and alkyl side-chain segments (g–i). Note that the intensity scales are the same for each plot. Intensities are shown on a logarithmic scale.

components, as we confirmed above, the diffraction images at 45° and 90° are principally influenced by the packing orientation of the side chains, while the 0° image is mainly influenced by the backbone orientation with some contributions of side-chain packing. Interestingly, the intensity of the (201) reflection in the 45° image appears to be enhanced by the interference between the backbone and side-chain components, as the simulation of the full polymer shows relatively intense peaks, while the simulations of the individual components show weaker diffraction spots.

The good agreement between the empirical and simulated GIXD data lends confidence in the structural model discussed thus far. However, there remain notable differences among the model and various empirical results in terms of the details of molecular packing—for instance, the tilt of the conjugated backbones or side chains with respect to the substrate and the in-plane rotation of the side chains relative to the backbones. We therefore investigated further how these molecular packing parameters affect the XRD patterns of the uniaxial films. First, we examined how the tilt of the backbones with respect to the substrate normal (14° simulation vs 20° NEXAFS) affects the simulated diffraction patterns. A unit cell containing only the backbone was considered, as it was noted above that the side chains do not contribute significantly to diffraction peaks arising from the polymer backbones. The backbone tilt was changed from 10° to 30° via 5° increments within a fixed unit cell. As shown in Figure 9, the (h10) intensity profile for the uniaxial polymer films are similar when the backbone tilt is <20°; the peak at lower Q_z appears more intense than the higher Q_z peaks. When the backbone tilt is >25°, however, the intensity of the higher Q_z peaks becomes much stronger, a result not consistent with experiment. We note that the energetic differences among these structural variations are minor. These results show that the (h10) peaks are relatively insensitive to the change in the backbone tilt when the tilt is <25°. Thus, the 6° difference in tilt between simulation and NEXAFS data is within the error bars, as there is no significant change in both the diffraction patterns and peak intensities with variation of the tilt in this range. These results reveal that there is likely considerable tilt disorder in the backbone tilt angles (ca. 0–20°). Importantly, this analysis shows the necessity and power of combining characterization methods to produce reliable structural models.

Second, in order to evaluate the effect of the side-chain orientation on the diffraction patterns, the tilt of the side chains in the unit cell was varied, though interdigitation between the side chains was maintained. These structures were not optimized, since after geometry optimization the tilt angle goes back to the original, energetically stable state. As the side-chain tilt changes from 26° to 31° and 36°, the in-plane rotation of the side chains from the backbones also changes from 58° to 85° and 86°. Figure 10 shows the XRD pattern of the full polymer with varying side chain tilt and that of only the side-chain part with peak indexes to clearly identify the diffraction peaks with respect to the tilt. As shown in Figure 10, the change of the side-chain tilt has a significant impact on the diffraction pattern. The simulated XRD patterns lose their agreement with the experimental pattern ($Q_{xy} \approx 0.5$–1.5 Å^{-1} and $Q_z \approx 0.0$–1.5 Å^{-1})

dx.doi.org/10.1021/ja210272z | J. Am. Chem. Soc. 2012, 134, 6177–6190

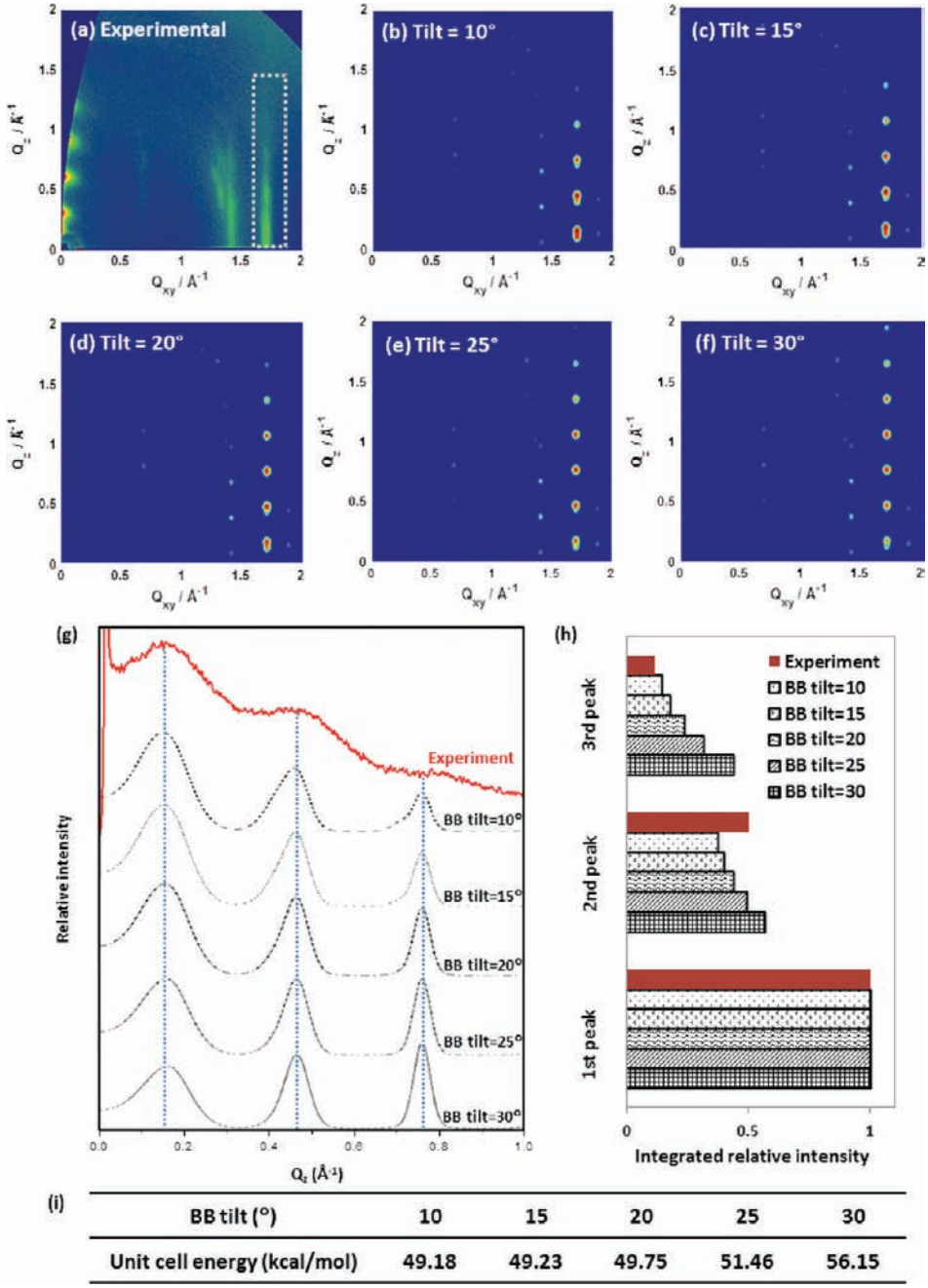

BB tilt (°)	10	15	20	25	30
Unit cell energy (kcal/mol)	49.18	49.23	49.75	51.46	56.15

Figure 9. Experimental (a) and simulated XRD patterns of uniaxial backbone with tilt (b) 10°, (c) 15°, (d) 20°, (e) 25°, and (f) 30°. The white dashed-line box in the experimental data indicates the diffraction pattern coming from the backbone contribution. (g) Plot of (h10) intensity of the peaks at Q_{xy} = 1.71 Å^{-1} vs Q_z. (h) Integrated relative intensity of the first, second, and third peaks of the experimental and simulated models with various backbone tilt angles. (i) Energy of the unit cell as a function of backbone tilt. For 2D GIXD, intensities are shown on a logarithmic scale.

as the side-chain tilt changes from 26° (tilt of the optimized model) to 31° or 36°. Since the side-chain orientation is related to the backbone orientation and lamellar thickness, artificial modification of the side-chain tilt angle with respect to the substrate normal may not be relevant to prove the exact tilt angle of the side chains. Nevertheless, these results suggest that the side-chain arrangements significantly influence the polymer packing and diffraction peak intensities and positions. The disagreement in side-chain orientation between the IR experiment and our XRD data/simulation likely arises from the exclusion from the simulation of both side-chain disorder and the possibility of gauche defects along the alkyl chains. Additionally, as mentioned earlier, the side-chain tilts extracted from polarized IR spectroscopy would overestimate the tilt angle for this system when disorder is present. The tilt angle extracted from the XRD measurements relates to the side chains in the interdigitated portion of the unit cell and is based on the assumption that the side-chain conformation is independent of side-chain length. The XRD measurement also points to having a non-interdigitated region about 3−5 methylenes long.[27] Such non-interdigitated regions do not appear in the simulations since the MM modeling does not

dx.doi.org/10.1021/ja210272z | J. Am. Chem. Soc. 2012, 134, 6177−6190

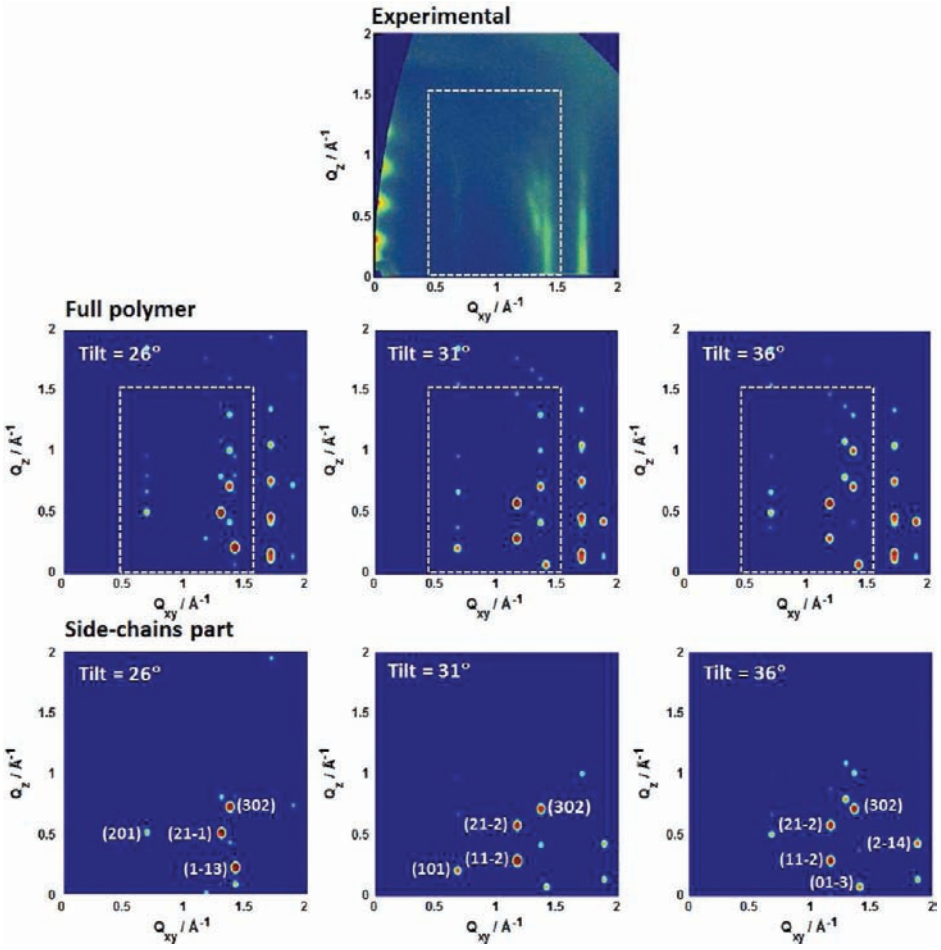

Figure 10. Experimental (top) and simulated 2D XRD patterns of the full polymer (middle) and of only the side-chain part (bottom) with side-chain tilts of 26°, 31°, and 36° in uniaxial PBTTT-C_{14} films. The white dotted-line box in the data points to the diffraction pattern coming from the side-chain contributions. Intensities are shown on a logarithmic scale.

include temperature-dependent contributions, which can result in an increase in the tilt angle when the *d*-spacing is held constant.

3.4. Influence of Alkyl Side-Chain Length on Polymer Packing. Variations in the alkyl side-chain length can have a profound impact both on polymer packing and orientation in thin films, which in turn can affect the macroscopic (opto)-electronic properties.[27,53] Empirically, the lateral ordering of the polymer films is nearly the same as the PBTTT-C_n side-chain length increases from C_{12} to C_{16}, while the lamellar thickness increases. Therefore, it is expected that longer side chains principally change the Q_z positions while Q_{xy} peak positions should be constant.

We determined the molecular structures of PBTTT with dodecyl (C_{12}) and hexadecyl (C_{16}) side chains to evaluate the influence of the side-chain length on the polymer packing properties (see the Supporting Information). The packing motifs of PBTTT determined with various side-chain lengths are shown in Table 3. In terms of the lamellar *d*-spacing, the simulated data show good agreement with the experimental data. Regardless of side-chain length, the polymer backbones are planar and tilt slightly with respect to the substrate normal to maintain strong inter-backbone interactions. The inter-digitated alkyl side chains are predicted to be straight and present a fully *trans*-conformation (though, as noted above, disorder and gauche defects likely appear in the actual thin films). On increasing the alkyl chain length, the size and shape of the polymer unit cells are modified slightly. With the addition of two methylenes, *a* increases by ~2 Å, resulting in increased lamellar *d*-spacing. The values of β, the angle between the polymer repeat direction (*c*) and the lamellae growth direction (*a*), and γ, the angle between the lamellae growth direction (*a*) and the backbone stacking direction (*b*), increase slightly by 1° and 3°, respectively. The inter-backbone distance overall remains constant and falls between 3.5 and 3.6 Å. The backbone tilt angle slightly decreases as the side chain

Table 3. Structural Parameters of the Simulated Unit Cells for PBTTT-C_n, n = 12, 14, and 16

	PBTTT-C_{12}	PBTTT-C_{14}	PBTTT-C_{16}
lattice parameters			
a (Å)	19.6	21.5	23.5
b (Å)	5.4	5.4	5.4
c (Å)	13.5	13.5	13.5
α (°)	137	137	137
β (°)	85	86	87
γ (°)	86	89	92
lamellar spacing (Å)	19.1	21.3	23.5
π-stacking distance (Å)	3.54	3.58	3.62
backbone tilt angle (°)	16	14	10
side-chain tilt angle (°)	25	26	27

dx.doi.org/10.1021/ja210272z | *J. Am. Chem. Soc.* 2012, 134, 6177–6190

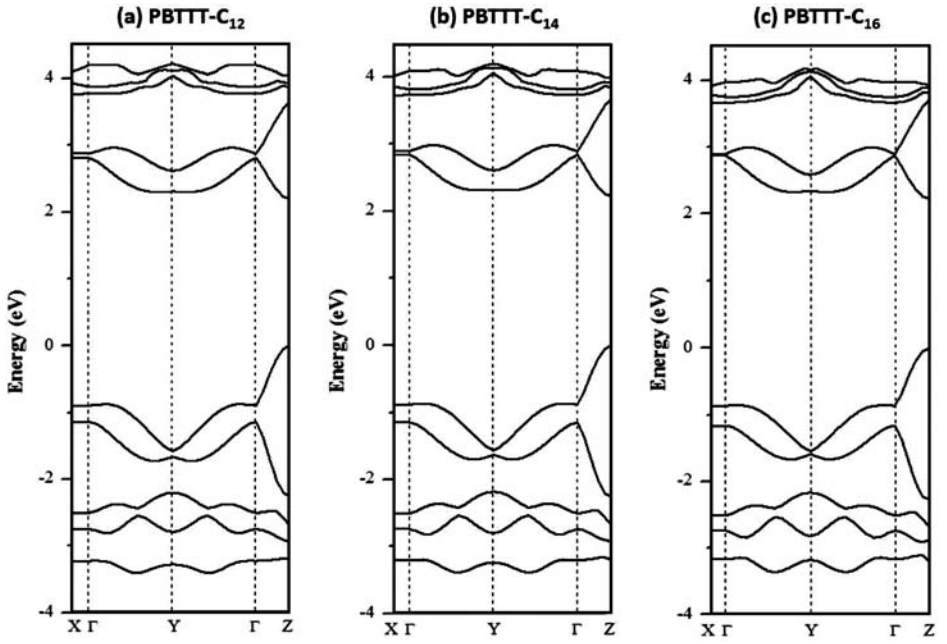

Figure 11. Electronic band structures of the PBTTT polymers with C_{12} (a), C_{14} (b), and C_{16} (c) side chains. Points of high symmetry in the first Brillouin zone are labeled as follows: Γ = (0,0,0), *X* = (0.5,0,0), *Y* = (0,0.5,0), *Z* = (0,0,0.5), all in crystallographic coordinates. The energy levels are shifted so that the top of the valence band represents the origin of the energy axis.

lengthens, which can be regarded as minimal-to-no change as it was shown that differences in backbone tilt produce negligible changes to the XRD patterns. The tilt of the side chains is also nearly the same with increasing side-chain length.

We note, however, that there is still a need to improve the models, in particular with regard to disorder. At the molecular level, disorder results from variation of both atomic displacements about their equilibrium positions and molecular/component orientations. These effects have been only marginally taken into account during the simulations presented here. First, the influence of thermal fluctuations is not included in the MM simulations as they are performed at 0 K. Additionally, in the process of energy minimization with 3D periodic boundary conditions, it is assumed that all surrounding cells are exact copies of the central unit cell. Recent works[52,54] by Rivnay et al. have shown that Warren–Averbach analysis of diffraction line shapes for PBTTT can provide insight into the nature of paracrystalline displacements and variations in the average lattice spacing—variations that are not taken into account in our model. Therefore, any larger-scale disorder is not properly represented. Molecular dynamics simulations of super cells are currently ongoing to investigate further the influence of disorder.

3.5. Electronic Properties as a Function of Alkyl Side-Chain Length. Efficient charge-carrier transport greatly depends on the polymer packing in the thin film.[55] Our simulations confirm the experimental results that PBTTT-C_n maintains relatively well-ordered crystalline domains with respect to the preferential orientation as the number of carbon atoms in the alkyl side chains increases from 12 to 16. It is expected that such well-ordered polymer structures can lead to efficient charge-carrier transport. By evaluating the band structure and intermolecular electronic couplings, the relationship between the 3D structure (taking into account the full alkyl side-chain lengths) and electronic properties of the polymers can be investigated.

The electronic band structures along the main reciprocal-space directions are displayed in Figure 11, with detailed information provided in Table 4. Here, the unit cell has one polymer unit, and five valence and conduction bands are displayed. The direct band gap, obtained at the *Z* point, is ~2.2 eV for each of the polymers in the series, a result consistent with experiment, 2.0 eV.[16] Along the *a*-axis (in the Γ*X* direction of the Brillouin zone), nearly flat bands are calculated, which means that there is no hole or electron transport among the polymer chains along the *a*-axis. On the other hand, large dispersions are found along other directions for both the valence and conduction bands. The strongest dispersions appear along the *c**-axis (in the Γ*Z* direction of the Brillouin zone), with widths of 0.9 eV for the valence band and 0.6 eV for the conduction band. Along the *b**-axis (in the Γ*Y* direction of the Brillouin zone), large dispersions are also observed, 0.7 eV for the valence band and 0.5 eV for the conduction band. When compared to the earlier work of Northrup,[29] the band dispersions determined here are smaller, a direct result of the backbone slip along the long molecular axis vs the cofacial backbone orientation considered in the previous study. Our results confirm that the band dispersion is larger along the polymer backbone than along the π-stacking direction, as one

Table 4. Calculated Band Gaps (E_g) at the *Z* Point and Dispersions of the Upper Valence Band (VB) and Lower Conduction Band (CB) along Various Directions in the Brillouin Zone of PBTTT-C_n, with *n* = 12, 14, and 16

	dispersion (eV)						
	X → Γ		Γ → *Y*		Γ → *Z*		
	VB	CB	VB	CB	VB	CB	E_g (eV)
PBTTT-C_{12}	0	0	0.68	0.50	0.89	0.61	2.20
PBTTT-C_{14}	0	0	0.68	0.52	0.88	0.62	2.22
PBTTT-C_{16}	0	0	0.68	0.53	0.87	0.65	2.22

dx.doi.org/10.1021/ja210272z | *J. Am. Chem. Soc.* 2012, 134, 6177–6190

might expect *a priori*, and are consistent with previous findings.[29]

Charge transport in spin-coated (disordered) thin films is usually described via a polaron hopping model in which localized charge carriers jump between adjacent chains.[56] In that context, Marcus theory[57,58] has been widely used to assess the charge-hopping rate between molecules or polymer chains.[48] According to semiclassical Marcus theory, the electron-transfer rate is given by

$$k_{ij} = \frac{2\pi}{\hbar} |t_{ij}|^2 \sqrt{\frac{1}{4\pi k_B T \lambda}} \exp\left[-\frac{(\lambda + \Delta G)^2}{4\lambda k_B T}\right] \quad (7)$$

where t_{ij} denotes the transfer integral (electronic coupling) between states i and j; λ, the reorganization energy; ΔG, the free energy difference between states i and j; k_B and h, Boltzmann's and Planck's constants, respectively; and T, the temperature. The magnitude of t_{ij} depends on the amount of overlap of the wave functions of the two states. Quantum-chemical calculations can provide direct insight into the extent of the transfer integrals for holes and electrons, t_h and t_e.

To further evaluate the electronic interactions in the polymer films, we evaluated the inter-chain electronic couplings between adjacent polymer chains at the B3LYP/6-31G(d,p) level of theory; the main results are collected in Table 5. The electronic couplings along the lamellar growth direction (a) are expectedly negligible, which is consistent with the lack of dispersion shown by the electronic band-structure calculations. Along the backbone stacking direction (b), there is substantial electronic coupling for both holes and electrons, 110−120 and 130−145 meV, respectively. These values are significant when compared to the electronic couplings found, for instance, in the pentacene crystal (~85 meV) for holes between adjacent molecules along the herringbone direction.[59,60] The coplanar character of the polymer backbones and the short intermolecular distances should result in large overlap between molecular orbitals on adjacent chains. In the context of a tight-binding model, these electronic-coupling values imply valence and conduction band widths along the b-axis on the order of 0.5 eV, which is consistent with the results of the band-structure calculations. The transfer integrals for PBTTT-C_{12} are similar to those determined by Brocorens et al.,[30] and smaller than those obtained by Milian-Medina et al. for polymers in a cofacial geometry.[61] The variations in band dispersions and transfer integrals when considering cofacial vs slipped polymer-chain packing underline the importance of having precise geometric models for the evaluation of the electronic properties. In any event, the results of the band structure and electronic coupling calculations provide a consistent picture and highlight pronounced electronic couplings for holes and electrons along both the intra- and inter-chain directions, which could provide for efficient intra- and inter-chain charge-carrier transport.

Table 5. Transfer Integrals for Holes (t_h) and Electrons (t_e) along the *b*-Axis for PBTTT as a Function of the Side-Chain Length

	b-axis	
dimer	$\lvert t_h \rvert$ (meV)	$\lvert t_e \rvert$ (meV)
PBTTT-C_{12}	113	130
PBTTT-C_{14}	115	139
PBTTT-C_{16}	119	145

No marked differences in the electronic couplings and band structures are obtained with respect to side-chain length (the electronic couplings and band dispersions increase slightly with longer side chains). This result points to the fact that the side chains are long enough to interdigitate and facilitate the formation of highly ordered lamellae, paving the way toward significant intermolecular/intramolecular electronic couplings.

4. CONCLUSIONS

We have used computational modeling to evaluate the three-dimensional orientation of PBTTT-C_{14} films by determining the optimal packing structure and unit-cell parameters based on experimental XRD patterns for uniaxial and biaxial polymer films. In terms of the polymer packing, planar backbones and relatively short inter-backbone distances are observed, leading to strong inter-chain interactions, as noted previously.[26,30] The straight and interdigitated alkyl side chains contribute to the formation of lamellar structures. Simulations of the diffraction patterns at in-plane angles (0°, 45°, 90°) with respect to the incident beam direction has allowed us to reveal the in-plane (bc) ordering, including substantial lateral slip among the conjugated backbones and considerable side-chain rotation relative to the backbones. This is noteworthy as it is the first time in-plane XRD simulations for biaxially oriented polymer structures have been demonstrated, and very reasonable agreement is found between experiment and theory.

We also examined the contributions of the individual polymer components to particular diffraction peaks in the XRD patterns. The ability to consider these components separately within the unit cell is a powerful technique to understand the diffraction patterns of uniaxial and biaxial films. From the analysis of the influence of the detailed molecular packing on the XRD patterns, it is clear that the observable diffraction patterns are more sensitive to the orientation of the alkyl side chains than the relative backbone orientation.

Finally, we thoroughly compared the geometric, packing, and electronic structures for PBTTT polymers with varying side chains, from C_{12} to C_{16}. Although slight changes in the lattice parameters are observed with increased side-chain length, the planarity and short inter-chain distance of the backbones remain nearly constant. Quantum-chemical calculations confirm that there is no substantial difference with regard to the electronic properties of the polymers as a function of side-chain length. Regardless of the chain length, large electronic couplings are found along the backbone-stacking direction. Strong band dispersions along both the polymer repeat direction and the backbone-stacking direction are observed, reflecting the potential for efficient inter- and intra-chain charge transport via a 2D channel. This suggests that as long as polymers have long-enough alkyl side chains to contribute to high-structural ordering, efficient intra- and inter-chain charge-carrier transport is possible.

In summary, the combination of computational and experimental techniques exploited in this work has demonstrated an ability to understand the intimate relationship between the structural and electronic properties of polymer films. These tools can foster rational design concepts for new molecular and polymeric materials for organic electronic applications.

dx.doi.org/10.1021/ja210272z | J. Am. Chem. Soc. 2012, 134, 6177−6190

■ ASSOCIATED CONTENT

Supporting Information

Force field evaluation for PBTTT-C_{12}, Figure S1 and Table S1; polymer component contribution to the XRD pattern of the uniaxial PBTTT-C_{14}, Figure S2; comparison of experimental and simulated packing structures of PBTTT-C_{12} and -C_{16}, Figure S3; and comparison between the presented and previous structural model of PBTTT-C_{12}, Table S2. This material is available free of charge via the Internet at http://pubs.acs.org.

■ AUTHOR INFORMATION

Corresponding Author

jean-luc.bredas@chemistry.gatech.edu

Present Address

[#]Department of Chemistry, Kyonggi University, Suwon 443-760, Korea

Notes

The authors declare no competing financial interest.

[⊗]Also affiliated with Department of Chemistry, King Abdulaziz University, Jeddah 21589, Saudi Arabia

■ ACKNOWLEDGMENTS

This work has been supported primarily by the Center for Advanced Molecular Photovoltaics (Award No. KUS-C1-015-21 made by King Abdullah University of Science and Technology, KAUST) as well as by the National Science Foundation under the STC program (Award DMR-0120967) and under the CRIF Program (Award CHE-0946869). Portions of this research were carried out at the Stanford Synchrotron Radiation Lightsource, a national user facility operated by Stanford University on behalf of the U.S. Department of Energy, Office of Basic Energy Sciences. The authors are grateful to Drs. Veaceslav Coropceanu and Lingyun Zhu for fruitful discussions. We also thank Drs. Martin Heeney and Iain McCulloch at Imperial College London for providing PBTTT samples.

■ REFERENCES

(1) Friend, R. H.; Gymer, R. W.; Holmes, A. B.; Burroughes, J. H.; Marks, R. N.; Taliani, C.; Bradley, D. D. C.; Dos Santos, D. A.; Bredas, J. L.; Logdlund, M.; Salaneck, W. R. *Nature* **1999**, *397*, 121.

(2) Kulkarni, A. P.; Tonzola, C. J.; Babel, A.; Jenekhe, S. A. *Chem. Mater.* **2004**, *16*, 4556.

(3) Sirringhaus, H. *Adv. Mater.* **2005**, *17*, 2411.

(4) McCulloch, I.; Heeney, M.; Chabinyc, M. L.; DeLongchamp, D.; Kline, R. J.; Coelle, M.; Duffy, W.; Fischer, D.; Gundlach, D.; Hamadani, B.; Hamilton, R.; Richter, L.; Salleo, A.; Shkunov, M.; Sporrowe, D.; Tierney, S.; Zhong, W. *Adv. Mater.* **2009**, *21*, 1091.

(5) Coakley, K. M.; McGehee, M. D. *Chem. Mater.* **2004**, *16*, 4533.

(6) Kroon, R.; Lenes, M.; Hummelen, J. C.; Blom, P. W. M.; De Boer, B. *Polym. Rev.* **2008**, *48*, 531.

(7) Chabinyc, M. L. *Polym. Rev.* **2008**, *48*, 463.

(8) Kline, R. J.; McGehee, M. D. *Polym. Rev.* **2006**, *46*, 27.

(9) Salleo, A.; Kline, R. J.; DeLongchamp, D. M.; Chabinyc, M. L. *Adv. Mater.* **2010**, *22*, 3812.

(10) Sirringhaus, H.; Tessler, N.; Friend, R. H. *Science* **1998**, *280*, 1741.

(11) Sirringhaus, H.; Brown, P. J.; Friend, R. H.; Nielsen, M. M.; Bechgaard, K.; Langeveld-Voss, B. M. W.; Spiering, A. J. H.; Janssen, R. A. J.; Meijer, E. W.; Herwig, P.; de Leeuw, D. M. *Nature* **1999**, *401*, 685.

(12) Rivnay, J.; Toney, M. F.; Zheng, Y.; Kauvar, I. V.; Chen, Z. H.; Wagner, V.; Facchetti, A.; Salleo, A. *Adv. Mater.* **2010**, *22*, 4359.

(13) Rivnay, J.; Steyrleuthner, R.; Jimison, L. H.; Casadei, A.; Chen, Z.; Toney, M. F.; Facchetti, A.; Neher, N.; Salleo, A. *Macromolecules* **2011**, *44*, 5246.

(14) Ma, W. L.; Yang, C. Y.; Gong, X.; Lee, K.; Heeger, A. J. *Adv. Funct. Mater.* **2005**, *15*, 1617.

(15) Kim, J. Y.; Kim, S. H.; Lee, H. H.; Lee, K.; Ma, W. L.; Gong, X.; Heeger, A. J. *Adv. Mater.* **2006**, *18*, 572.

(16) McCulloch, I.; Heeney, M.; Bailey, C.; Genevicius, K.; Macdonald, I.; Shkunov, M.; Sparrowe, D.; Tierney, S.; Wagner, R.; Zhang, W. M.; Chabinyc, M. L.; Kline, R. J.; McGehee, M. D.; Toney, M. F. *Nat. Mater.* **2006**, *5*, 328.

(17) Chabinyc, M. L.; Toney, M. F.; Kline, R. J.; McCulloch, I.; Heeney, M. *J. Am. Chem. Soc.* **2007**, *129*, 3226.

(18) Wang, S.; Tang, J. C.; Zhao, L. H.; Png, R. Q.; Wong, L. Y.; Chia, P. J.; Chan, H. S. O.; Ho, P. K. H.; Chua, L. L. *Appl. Phys. Lett.* **2008**, *93*, 162103.

(19) Rawcliffe, R.; Shkunov, M.; Heeney, M.; Tierney, S.; McCulloch, I.; Campbell, A. *Chem. Commun.* **2008**, 871.

(20) Esenturk, O.; Kline, R. J.; Deongchamp, D. M.; Heilweil, E. J. *J. Phys. Chem. C* **2008**, *112*, 10587.

(21) Jung, Y.; Kline, R. J.; Fischer, D. A.; Lin, E. K.; Heeney, M.; McCulloch, I.; DeLongchamp, D. M. *Adv. Funct. Mater.* **2008**, *18*, 742.

(22) Hamadani, B. H.; Gundlach, D. J.; McCulloch, I.; Heeney, M. *Appl. Phys. Lett.* **2007**, *91*, 243512.

(23) Umeda, T.; Kumaki, D.; Tokito, S. *J. Appl. Phys.* **2009**, *105*, 024516.

(24) Parmer, J. E.; Mayer, A. C.; Hardin, B. E.; Scully, S. R.; McGehee, M. D.; Heeney, M.; McCulloch, I. *Appl. Phys. Lett.* **2008**, *92*, 113309.

(25) Mayer, A. C.; Toney, M. F.; Scully, S. R.; Rivnay, J.; Brabec, C. J.; Scharber, M.; Koppe, M.; Heeney, M.; McCulloch, I.; McGehee, M. D. *Adv. Funct. Mater.* **2009**, *19*, 1173.

(26) DeLongchamp, D. M.; Kline, R. J.; Lin, E. K.; Fischer, D. A.; Richter, L. J.; Lucas, L. A.; Heeney, M.; McCulloch, I.; Northrup, J. E. *Adv. Mater.* **2007**, *19*, 833.

(27) Kline, R. J.; DeLongchamp, D. M.; Fischer, D. A.; Lin, E. K.; Richter, L. J.; Chabinyc, M. L.; Toney, M. F.; Heeney, M.; McCulloch, I. *Macromolecules* **2007**, *40*, 7960.

(28) DeLongchamp, D. M.; Kline, R. J.; Jung, Y.; Lin, E. K.; Fischer, D. A.; Gundlach, D. J.; Cotts, S. K.; Moad, A. J.; Richter, L. J.; Toney, M. F.; Heeney, M.; McCulloch, I. *Macromolecules* **2008**, *41*, 5709.

(29) Northrup, J. E. *Phys. Rev. B* **2007**, *76*, 245202.

(30) Brocorens, P.; Van Vooren, A.; Chabinyc, M. L.; Toney, M. F.; Shkunov, M.; Heeney, M.; McCulloch, I.; Cornil, J.; Lazzaroni, R. *Adv. Mater.* **2009**, *21*, 1193.

(31) DeLongchamp, D. M.; Kline, R. J.; Jung, Y.; Germack, D. S.; Lin, E. K.; Moad, A. J.; Richter, L. J.; Toney, M. F.; Heeney, M.; McCulloch, I. *ACS Nano* **2009**, *3*, 780.

(32) Rappe, A. K.; Casewit, C. J.; Colwell, K. S.; Goddard, W. A.; Skiff, W. M. *J. Am. Chem. Soc.* **1992**, *114*, 10024.

(33) Sun, H.; Ren, P.; Fried, J. R. *Comput. Theor. Polym. Sci.* **1998**, *8*, 229.

(34) Mayo, S. L.; Olafson, B. D.; Goddard, W. A. *J. Phys. Chem.* **1990**, *94*, 8897.

(35) Ewald, P. P. *Ann. Phys.* **1921**, *64*, 253.

(36) Breiby, D. W.; Bunk, O.; Andreasen, J. W.; Lemke, H. T.; Nielsen, M. M. *J. Appl. Crystallogr.* **2008**, *41*, 262.

(37) Breiby, D. W.; Chin, P. T. K.; Andreasen, J. W.; Grimsrud, K. A.; Di, Z. Y.; Janssen, R. A. J. *Langmuir* **2009**, *25*, 10970.

(38) Smilgies, D. M. *Rev. Sci. Instrum.* **2002**, *73*, 1706.

(39) Becke, A. D. *Phys. Rev. A* **1988**, *38*, 3098.

(40) Becke, A. D. *J. Chem. Phys.* **1993**, *98*, 5648.

(41) Lee, C.; Yang, W.; Parr, R. G. *Phys. Rev. B* **1988**, *37*, 785.

(42) Hariharan, P. C.; Pople, J. A. *Theor. Chim. Acta* **1973**, *28*, 213.

(43) Francl, M. M.; Petro, W. J.; Hehre, W. J.; Binkley, J. S.; Gordon, M. S.; DeFrees, D. J.; Pople, J. A. *J. Chem. Phys.* **1982**, *77*, 3654.

(44) Rassolov, V. A.; Pople, J. A.; Ratner, M. A.; Windus, T. L. *J. Chem. Phys.* **1998**, *109*, 1223.

(45) Valeev, E. F.; Coropceanu, V.; da Silva, D. A.; Salman, S.; Bredas, J. L. *J. Am. Chem. Soc.* **2006**, *128*, 9882.
(46) Frisch, M. J.; Trucks, G. W.; Schlegel, H. B.; Scuseria, G. E.; Robb, M. A.; Cheeseman, J. R.; Scalmani, G.; Barone, V.; Mennucci, B.; Petersson, G. A.; Nakatsuji, H.; Caricato, M.; Li, X.; Hratchian, H. P.; Izmaylov, A. F.; Bloino, J.; Zheng, G.; Sonnenberg, J. L.; Hada, M.; Ehara, M.; Toyota, K.; Fukuda, R.; Hasegawa, J.; Ishida, M.; Nakajima, T.; Honda, Y.; Kitao, O.; Nakai, H.; Vreven, T.; Montgomery, J. J. A.; Peralta, J. E.; Ogliaro, F.; Bearpark, M.; Heyd, J. J.; Brothers, E.; Kudin, K. N.; Staroverov, V. N.; Kobayashi, R.; Normand, J.; Raghavachari, K.; Rendell, A.; Burant, J. C.; Iyengar, S. S.; Tomasi, J.; Cossi, M.; Rega, N.; Millam, J. M.; Klene, M.; Knox, J. E.; Cross, J. B.; Bakken, V.; Adamo, C.; Jaramillo, J.; Gomperts, R.; Stratmann, R. E.; Yazyev, O.; Austin, A. J.; Cammi, R.; Pomelli, C.; Ochterski, J. W.; Martin, R. L.; Morokuma, K.; Zakrzewski, V. G.; Voth, G. A.; Salvador, P.; Dannenberg, J. J.; Dapprich, S.; Daniels, A. D.; Farkas, Ö.; Foresman, J. B.; Ortiz, J. V.; Cioslowski, J.; Fox, D. J. *Gaussian 09*, Revision A.02; Gaussian, Inc.: Wallingford, CT, 2009.
(47) Dovesi, R.; Saunders, V. R.; Roetti, C.; Orlando, R.; Zicovich-Wilson, C. M.; Pascale, F.; Civalleri, B.; Doll, K.; Harrison, N. M.; Bush, I. J.; D'Arco, P.; Llunell, M. *CRYSTAL06*; University of Torino: Torino, Italy, 2006.
(48) Coropceanu, V.; Cornil, J.; da Silva, D. A.; Olivier, Y.; Silbey, R.; Bredas, J. L. *Chem. Rev.* **2007**, *107*, 926.
(49) Baker, J. L.; Jimison, L. H.; Mannsfeld, S.; Volkman, S.; Yin, S.; Subramanian, V.; Salleo, A.; Alivisatos, A. P.; Toney, M. F. *Langmuir* **2010**, *26*, 9146.
(50) The crystal domains in the simulations are preferentially oriented with a^* perpendicular to the substrate plane, and the GIXD geometry does not allow for the out-of-plane reciprocal lattice vector to intersect the Ewald sphere, resulting in no (h00) Bragg peaks in the simulated XRDs patterns.
(51) We note that both Figure 6 and Table 2 show good agreement between experiment and simulation. They do differ, however, in that Figure 6 shows the intensities but only the approximate peak positions (which have to be read from the plot), while Table 2 accurately gives the peak positions (accurate to ± 0.01 Å^{-1}).
(52) Rivnay, J.; Noriega, R.; Northrup, J. E.; Kline, R. J.; Toney, M. F.; Salleo, A. *Phys. Rev. B* **2011**, *83*, 121306.
(53) Szarko, J. M.; Guo, J. C.; Liang, Y. Y.; Lee, B.; Rolczynski, B. S.; Strzalka, J.; Xu, T.; Loser, S.; Marks, T. J.; Yu, L. P.; Chen, L. X. *Adv. Mater.* **2010**, *22*, 5468.
(54) Rivnay, J.; Noriega, R.; Kline, R. J.; Salleo, A.; Toney, M. F. *Phys. Rev. B* **2011**, *84*, 045203.
(55) Bredas, J. L.; Calbert, J. P.; da Silva, D. A.; Cornil, J. *Proc. Natl. Acad. Sci. U.S.A.* **2002**, *99*, 5804.
(56) Bredas, J. L.; Beljonne, D.; Coropceanu, V.; Cornil, J. *Chem. Rev.* **2004**, *104*, 4971.
(57) Marcus, R. A. *Rev. Mod. Phys.* **1993**, *65*, 599.
(58) Marcus, R. A.; Sutin, N. *Biochim. Biophys. Acta* **1985**, *811*, 265.
(59) Endres, R. G.; Fong, C. Y.; Yang, L. H.; Witte, G.; Woll, C. *Comput. Mater. Sci.* **2004**, *29*, 362.
(60) Gruhn, N. E.; da Silva, D. A.; Bill, T. G.; Malagoli, M.; Coropceanu, V.; Kahn, A.; Bredas, J. L. *J. Am. Chem. Soc.* **2002**, *124*, 7918.
(61) Milian-Medina, B.; Van Vooren, A.; Brocorens, P.; Gierschner, J.; Shkunov, M.; Heeney, M.; McCulloch, I.; Lazzaroni, R.; Cornil, J. *Chem. Mater.* **2007**, *19*, 4949.